# Constitutive Modeling of Porous Hydrate-Crowned Liquid Films for Dynamic Interfacial Area and Film Thickness Prediction in Gas Pipelines

[1]Kefas Odofori, [2]Owei L. Youpele, [3]Dr. BlessingZekieni Yelebe

*[1,2,3]Niger Delta University*

***Abstract-*** ***We propose a constitutive modeling framework that replaces conventional sharp-interface film thickness correlations with a dynamic, multi-scale system for predicting gas-water interfacial area and liquid film evolution in deepwater gas pipelines. The core novelty lies in explicitly coupling hydrate nucleation and crystal growth to interfacial rheology, thereby capturing the feedback between microstructure and macroscopic film behavior. The proposed system integrates four interconnected modules: a neural network emulator trained on interfacial Langmuir trough experiments to output viscoelastic moduli and yield stress, a discrete element method crust morphology simulator that maps crystal packing porosity to mechanical strength, a porous hydrate crust constitutive law expressing effective viscosity as a function of porosity and shear rate, and a modified thin-film lubrication solver that incorporates these rheological closures. In this framework, the gas-water interface is no longer treated as a sharp discontinuity with constant tension; instead, it behaves as a viscoplastic material whose properties evolve with subcooling, film Reynolds number, and local porosity. The porosity itself is governed by a dynamic population balance that tracks hydrate mass deposition from the gas phase. We solve the coupled lubrication and porosity equations using a fully implicit finite-volume method, with the neural network and discrete element simulations providing closure relations at each time step. Our approach enables transient prediction of film thinning, crust formation, and interfacial area evolution under stratified, annular, or slug flow regimes. The primary contributions are the introduction of a porosity-dependent yield stress derived from percolation theory, the replacement of static film correlations with a causally coupled rheological film model, and the demonstration of direct interchange between microscale crystal packing and macroscale film dynamics. This framework significantly improves fidelity in hydrate risk assessment for subsea pipelines.***

***Index-Terms - Modeling, Porous, Hydrate, Crowned, Dynamic, Interfacial, Films, Thickness, Predictions, Pipelines***

## I. INTRODUCTION

The transportation of unprocessed natural gas in deepwater subsea pipelines is profoundly challenged by the formation of gas hydrates, crystalline solids that can nucleate, grow, agglomerate, and ultimately plug the flow path. This phenomenon represents one of the most persistent threats to flow assurance in offshore oil and gas operations, as hydrate plugs can cause catastrophic production shutdowns and necessitate costly remediation procedures (Bomba et al., 2018). Conventional strategies for managing hydrate risks have predominantly relied on thermodynamic inhibition, such as injecting large volumes of methanol or monoethylene glycol, or on the application of low-dosage hydrate inhibitors (LDHIs) that kinetically delay nucleation or prevent agglomeration (M. Zhang et al., 2025). These chemical approaches, however, impose significant economic and environmental penalties, especially in long-distance tiebacks and high-water-cut systems.

From an engineering modeling perspective, multiphase flow assurance tools have historically treated the gas-water interface as a clean, stress-free boundary with a constant surface tension (Li et al., 2024) (Shippen & Bailey, 2012). Liquid film thickness in annular flow, for example, is often estimated using empirical correlations derived from conductance probe measurements or through simplified lubrication theory approximations that neglect the presence of solid deposits (Okawa et al., 2010). Similarly, the prediction of interfacial area—a critical parameter for mass transfer calculations—relies on geometric flow regime maps or population balance models that do not account for the mechanical alteration of the interface by hydrate crystals (Bhole et al., 2008) (Brunner et al., 1983). A substantial gap therefore exists between the micro-scale physics of hydrate formation and the macro-scale hydrodynamic models used for pipeline design and operation.

Recent advances in the physics of hydrate-laden interfaces have begun to bridge this divide. Interfacial stress rheometry (ISR), a technique originally developed to characterize surfactant-adsorbed films (Fuller & Vermant, 2012), has been adapted to quantify the viscoelastic properties of particle-laden and crystalline interfaces (Garbin, 2019). Parallel developments in the discrete element method (DEM) have enabled the simulation of particle packing and force chain networks within jammed layers at fluid interfaces (Kacianauskas et al., 2007) (Ji et al., 2020). These micro-scale studies reveal that a porous hydrate crust behaves like a soft glassy material: it exhibits a measurable yield stress, a strain-dependent modulus, and a complex viscoelastic response that evolves with crystal packing density and subcooling. Critically, these rheological transformations modify the hydrodynamic boundary condition at the gas-water interface, thereby altering the film stability, the interfacial shear stress, and the overall flow regime.

Despite these experimental and computational advances, existing hydrate risk assessment models in multiphase flow simulators continue to either ignore the rheological impact of the crust entirely or approximate it through a constant, empirically determined friction factor (Hegde et al., 2015)

(Danielson, 2012). No comprehensive framework exists that explicitly couples the micro-scale evolution of the porous hydrate crust to the macro-scale dynamics of the liquid film. The present study aims to fill this void by proposing a constitutive modeling framework that replaces the conventional sharp-interface approach with a dynamic, porosity-coupled rheological model. Our core hypothesis is that the packing density of nucleating hydrate crystals governs the viscoelastic response of the interface, and that this response, in turn, dictates the temporal evolution of film thickness and interfacial area under transient flow conditions.

We propose an integrated methodology that combines interfacial stress rheometry (ISR) experiments with discrete element method (DEM) simulations to quantify how hydrate crystals modify the interfacial stress-strain behavior. The resulting data are used to formulate a two-parameter constitutive law: the effective viscosity of the hydrate-crowned interface is expressed as a function of porosity and local shear rate, while the yield stress follows a percolation-type scaling derived from granular physics. These rheological closures are then embedded into a thin-film lubrication framework, extending classical film evolution equations to account for the porosity-dependent resistance to deformation. The porosity field itself evolves via a dynamic population balance model that advects and deposits hydrate mass from the supersaturated gas phase. By solving the coupled system of film thickness, porosity, and rheology equations using a fully implicit finite-volume method, we can predict transient film thinning, crust formation, and interfacial area evolution under stratified, annular, or slug flow regimes.

The primary contributions of this work are threefold. First, we introduce a porosity-dependent yield stress relationship for hydrate-laden interfaces that emerges from percolation theory and is validated against ISR and DEM data. Second, we replace static empirical film correlations with a causally coupled rheological film model that dynamically evolves with hydrate deposition. Third, we demonstrate a direct and computationally feasible interchange between micro-scale crystal packing simulations and macro-scale film dynamics, thereby creating a multi-scale modeling pipeline for improved hydrate plugging risk assessment. The remainder of this paper is organized as follows: Section 2 reviews related work in multiphase flow assurance, hydrate kinetics, and interfacial rheology. Section 3 describes the physicochemical basis of hydrate interfacial rheology, including nucleation mechanisms and crust morphology. Section 4 details the coupled ISR-DEM methodology and the development of the porosity-dependent constitutive law. Section 5 presents experimental and computational results, including validation against film thickness measurements and flow loop observations. Section 6 discusses the implications for transient pipeline operations, model limitations, and directions for future work. Section 7 concludes the paper.

## RELATED WORK

The modeling of hydrate formation and deposition in multiphase pipelines has historically been pursued along two largely independent trajectories: the thermodynamic and kinetic modeling of hydrate nucleation and growth, and the hydrodynamic modeling of multiphase flow regimes and liquid film behavior. A comprehensive review of hydrate risk in natural gas transportation

identifies the critical need to bridge these domains, particularly in deepwater environments where subcooling and residence times are conducive to rapid plugging (Zhao et al., 2023). Existing flow assurance strategies, such as the application of thermodynamic hydrate inhibitors (THIs) or low-dosage kinetic inhibitors (KHIs), are often designed using thermodynamic phase equilibrium models that predict the hydrate formation envelope without considering the dynamic feedback between crystal growth and the evolving multiphase flow field (M. Zhang et al., 2025).

From the perspective of multiphase flow modeling, a variety of approaches have been developed to predict flow regimes, liquid holdup, and film thickness in gas-dominated pipelines. Two-fluid models, which solve separate conservation equations for each phase, typically employ empirical closure relations for interfacial friction and wall shear (Li et al., 2024). In annular flow, for example, the liquid film thickness is often estimated using correlations such as the Henstock-Hanratty relationship, which correlates film thickness to a dimensionless gas flow rate under the assumption of a smooth, stress-free interface (Okawa et al., 2010). However, these correlations were developed for clean systems and do not account for the mechanical effect of a deposited hydrate crust, which can significantly alter the interfacial boundary condition. Similarly, drift-flux models, commonly used for transient pipeline simulations, predict gas and liquid velocities using empirical slip relationships and flow regime maps, but these maps are typically derived from experiments with inert, non-depositing fluids (Shippen & Bailey, 2012).

Several recent studies have attempted to incorporate the physics of hydrate deposition into multiphase flow models. For instance, a hydrate deposition model for gas-dominant systems explicitly tracks the growth of a hydrate layer on the pipe wall, using a mass transfer coefficient derived from the turbulent boundary layer (S. Zhang et al., 2022). While this approach captures the evolution of a solid deposit thickness, it treats the hydrate layer as a fully consolidated solid with a constant, high mechanical strength, and does not consider the porous, fragile crust that forms at the gas-water interface before deposition occurs. Other models simulate hydrate agglomeration and plugging by coupling a population balance for particle size distribution with a pressure drop calculation (Rao, 2013). However, these population balance frameworks typically simplify the liquid film as a uniform slurry and neglect the spatial and temporal heterogeneity of the interface.

A parallel body of literature has focused on the rheology of particle-laden fluid interfaces, a topic of fundamental importance for the current work. Experimental studies using Langmuir troughs and interfacial stress rheometers have characterized the viscoelastic response of interfaces laden with colloidal particles, nanoparticles, and Janus particles (Qiao et al., 2022). These experiments demonstrate that as the surface coverage approaches jamming, the interface transitions from a viscous fluid to an elastic solid, exhibiting a yield stress and a strain-dependent modulus. The concept of a jammed particle layer at a fluid interface has also been explored theoretically using granular physics and percolation theory, providing scaling laws that relate the yield stress to the area fraction of particles see e.g., the approach in. Moreover, techniques originally developed for bulk colloidal suspensions, such as the Krieger-Dougherty relation, have been adapted to describe the effective viscosity of particle-laden films, accounting for the hydrodynamic interactions between particles under shear (Lalieu, 2023).

Within the specific context of hydrates, interfacial stress rheometry has been applied to study cyclopentane hydrate slurries, revealing that a growing hydrate crust imparts a measurable storage modulus to the interface, indicative of a solid-like network (Fuller & Vermant, 2012). Discrete element method simulations of particle sintering at fluid interfaces have also been used to study the effect of attractive capillary bridges on the cohesive strength of the crust (Kacianauskas et al., 2007). While these micro-scale studies provide essential mechanistic insights, they have not yet been integrated into a predictive framework for pipeline-scale film dynamics.

The key novelty of the proposed approach, compared to the existing literature, lies in the explicit coupling of micro-scale interfacial rheology—derived from ISR experiments and DEM simulations—into a macro-scale thin-film lubrication solver. While prior works have either focused on the thermodynamics of hydrate formation, the hydrodynamics of multiphase flow, or the rheology of particle-laden interfaces in isolation, no existing model provides a dynamic, porosity-aware constitutive law for the gas-water interface that evolves with hydrate deposition and feeds back into film thickness and interfacial area predictions. Our framework replaces static film correlations and constant surface tension assumptions with a causally coupled system, where the packing density of nucleating hydrate crystals governs the viscoelastic resistance to film deformation, and the film evolution, in turn, controls the rate of hydrate mass transfer and deposition. This integration represents a significant step forward in fidelity for transient hydrate risk assessment in deepwater pipelines.

## PHYSICOCHEMICAL BASIS OF HYDRATE INTERFACIAL RHEOLOGY

Understanding the rheological transformation of the gas-water interface induced by hydrate formation requires an examination of the underlying physicochemical mechanisms. Hydrate nucleation and growth at fluid interfaces are fundamentally distinct from bulk crystallization processes, as the interface provides a geometrically confined environment that lowers the free energy barrier for nucleation and facilitates the assembly of porous, polycrystalline crusts. A hydrate crystal forms when water and guest molecules (e.g., methane, ethane, or cyclopentane) arrange into a clathrate cage structure under conditions of elevated pressure and low temperature, known as the hydrate stability zone (Jr & Koh, 2007). The interfacial region, characterized by a sharp gradient in chemical potential and the availability of both water and guest molecules, serves as a preferential nucleation site, leading to the rapid formation of a thin, solid-like film at the gas-water contact.

The resulting hydrate crust is not a dense, impermeable solid but rather a porous, granular material composed of micron-scale crystallites that sinter together through capillary bridges and interparticle attractive forces (S. Zhang et al., 2022). The porosity of this crust—defined as the fraction of void space within the crystal network—critically governs its mechanical response to applied stress. Porosity in hydrate crusts arises from several sources: incomplete surface coverage during nucleation, the dendritic growth morphology induced by rapid mass transfer, and the geometric constraints of packing non-spherical crystallites onto a curved interface. Measurements

obtained from cryo-scanning electron microscopy (cryo-SEM) of cyclopentane hydrates, for example, reveal porosities ranging from 0.15 to 0.45, depending on the subcooling and the presence of surfactants or inhibitors (Murshed et al., 2008). This porosity dictates the connectivity of the force-bearing network within the crust, which in turn determines its bulk viscoelastic properties.

From a rheological perspective, a porous hydrate crust behaves analogously to a jammed granular material. As the packing density of crystallites increases—i.e., as porosity decreases—the number of particle-particle contacts per unit volume rises, forming a percolating network that can support shear stress. This transition is characterized by a yield stress, $\tau_y$, below which the crust deforms elastically and above which it flows like a viscous fluid see, e.g., the granular physics analysis in. The yield stress is not a material constant but rather a function of the local porosity, $\phi$:

$$\tau_y(\phi) = \tau_0 \left(\frac{\phi_c - \phi}{\phi_c}\right)^{-\beta} \quad \text{for } \phi < \phi_c \qquad (1)$$

where $\phi_c$ is the critical porosity at which the force-bearing network becomes percolating (typically around 0.3–0.5 for random packings of irregular particles), $\tau_0$ is a reference stress scale that depends on the inter-crystallite adhesion strength and the contact area, and $\beta$ is a percolation exponent (theoretically predicted to be approximately 2.0–2.5 for three-dimensional packed systems) (Sahimi & Goddard, 1986). Equation 1 implies that as the crust becomes denser (i.e., as $\phi$ decreases toward $\phi_c$ ), the yield stress increases dramatically, rendering the interface increasingly resistant to deformation.

In addition to the yield stress, the effective viscosity of the hydrate-crowned interface, $\eta_{\text{eff}}$, also evolves with porosity and the applied shear rate. Below the yield stress, the interface behaves as a viscoelastic solid, characterized by a storage modulus, $G'$, and a loss modulus, $G''$, which can be measured using interfacial stress rheometry (ISR) (Fuller & Vermant, 2012). Above the yield stress, the crust undergoes plastic flow, and the effective viscosity follows a shear-thinning relationship analogous to that observed in dense colloidal suspensions:

$$\eta_{\text{eff}}(\phi, \dot{\gamma}) = \eta_s \left(1 - \frac{\phi}{\phi_m}\right)^{-2} \left(\frac{\dot{\gamma}}{\dot{\gamma}_0}\right)^{n-1} \qquad (2)$$

where $\eta_s$ is the viscosity of the suspending fluid (the liquid sublayer), $\phi_m$ is the maximum packing fraction (typically 0.64 for random close packing of monodisperse spheres), $\dot{\gamma}$ is the local shear rate, $\dot{\gamma}_0$ is a reference shear rate, and $n$ is a power-law exponent (empirically found to be around 0.5–0.8 for hydrate slurries) (Jogun & Zukoski, 1996) (Lalieu, 2023). The term $(1 - \phi/\phi_m)^{-2}$ is the Krieger-Dougherty-like divergence that captures the dramatic increase in viscosity as porosity decreases and the packing approaches maximum density. The shear-thinning term, $(\dot{\gamma}/\dot{\gamma}_0)^{n-1}$, accounts for the breakdown of particle clusters and the alignment of crystallites under high shear, which reduces the effective resistance.

The interplay between porosity-dependent yield stress and effective viscosity governs the hydrodynamic boundary condition at the gas-water interface. In a standard thin-film lubrication model, the interface is assumed to be stress-free, meaning that the shear stress at the interface is

zero, $\tau_{\text{interface}} = 0$. However, when a hydrate crust is present, the interface can sustain a finite shear stress, and the boundary condition becomes:

$$\tau_{\text{interface}} = \begin{cases} \eta_{\text{eff}}\dot{\gamma} & \text{if } |\tau| > \tau_y(\phi) \\ G'\gamma & \text{if } |\tau| \leq \tau_y(\phi) \end{cases} \quad (3)$$

where $\tau$ is the applied shear stress from the gas phase and the liquid film, and $\gamma$ is the elastic strain. This non-linear boundary condition introduces a feedback loop: if the gas-induced shear stress is below the yield stress of the crust, the interface behaves as a no-slip or partial-slip boundary, impeding the shearing of the underlying liquid film. This can lead to film thickening or even stagnation, promoting further hydrate deposition. Conversely, if the shear stress exceeds the yield stress, the crust yields plastically, allowing the interface to deform and the film to thin. The evolving porosity, $\phi$, thus acts as a state variable that dynamically modulates the mechanical properties of the interface, directly linking micro-scale crystal packing to macro-scale film dynamics.

Furthermore, the porosity itself is not static but evolves through the simultaneous processes of hydrate mass deposition, crystal sintering, and mechanical erosion. A population balance model is required to track the time-dependent change in crust porosity, $\partial\phi/\partial t$, as a function of the net hydrate mass flux to the interface, the rate of inter-crystallite sintering, and the rate of mechanical breakup due to shear (Bhole et al., 2008). This multi-scale coupling—where the interface rheology depends on porosity, porosity evolves with mass transfer, and mass transfer is modulated by the film hydrodynamics—constitutes the core of the constitutive modeling framework proposed in this work. By replacing the conventional assumption of a sharp, stress-free interface with a porosity-dependent viscoplastic boundary condition, we can significantly improve the predictive capability for transient film evolution and interfacial area under realistic pipeline conditions.

Coupled ISR-DEM Methodology for Hydrate-Laden Interfaces

To translate the physicochemical principles described above into a predictive computational framework, we develop a coupled methodology that integrates interfacial stress rheometry and discrete element method simulations. The objective is to quantify the porosity-dependent viscoelastic response of hydrate-crowned gas-water interfaces and to embed these rheological closure relations into a thin-film lubrication solver. Our approach proceeds through three sequential stages: first, we conduct systematic ISR experiments to measure the storage modulus, loss modulus, and yield stress of hydrate-laden interfaces as functions of subcooling and initial crystal seed density; second, we perform DEM simulations to resolve the microstructural packing of crystallites within the crust and to extract porosity-dependent mechanical properties that are difficult to measure directly; third, we combine the ISR and DEM data into a unified constitutive law that can be expressed as a function of a single state variable—the local crust porosity.

Interfacial Stress Rheometry Protocol

The ISR experiments are performed using a custom-built Langmuir trough equipped with a magnetic needle rheometer, following established protocols for particle-laden interfaces (Fuller &

Vermant, 2012). The trough contains a quiescent water sublayer (deionized water, resistivity 18.2 MΩ·cm) maintained at a constant temperature of 4°C, which lies within the hydrate stability zone for methane at atmospheric pressure when the headspace is pressurized. A cyclopentane hydrate system is used as a model because cyclopentane forms Structure II hydrate at atmospheric pressure and moderate subcooling, thereby avoiding the need for high-pressure ISR equipment. Cyclopentane (99% purity) is layered on top of the water sublayer at a constant oil-to-water volume ratio of 0.2, and the system is cooled to a subcooling of $\Delta T = \mathrm{T}_{eq} - \mathrm{T}_{exp}$, where $\mathrm{T}_{eq} \approx 7.8$°C is the equilibrium temperature for cyclopentane hydrate.

Hydrate nucleation is initiated by injecting a pre-formed cyclopentane hydrate slurry (seed density $\phi_0$) into the interface. The storage modulus $G'(\omega)$ and loss modulus $G''(\omega)$ are measured over a frequency range of $\omega = 0.1$ to 10 rad·s$^{-1}$ using oscillatory shear at a strain amplitude of 0.1% (within the linear viscoelastic regime). A creep test is then performed by applying a constant torque to the magnetic needle and recording the angular displacement; the yield stress $\tau_y$ is identified as the critical stress at which the interface transitions from elastic (recoverable) to viscous (irrecoverable) deformation. The complete dataset, collected for 5 different seed densities $\phi_0$ (0.05, 0.10, 0.15, 0.20, 0.25) and 3 subcooling levels $\Delta T$ (2, 4, 6 K), comprises 15 experimental conditions, each replicated three times. This dataset forms the training set for the neural network emulator described in Section 4.3.

Discrete Element Method Simulation of Crust Microstructure

While ISR provides direct measurements of the macroscopic rheological response, it cannot resolve the internal packing structure of the porous hydrate crust. To establish a quantitative relationship between porosity and mechanical properties, we conduct DEM simulations using the open-source code LIGGGHTS (Kozicki & Donze, 2009). Each simulation represents a small, representative volume element of the crust as a collection of 5,000 to 20,000 spherical particles (mean diameter $d_p = 10$ μm, with a log-normal size distribution of polydispersity index 0.2) confined between two planar walls. The particles interact via a Hertzian normal contact law and a Cundall-Strack tangential friction model, with material properties representative of cyclopentane hydrate: Young's modulus $E = 1.0$ GPa, Poisson's ratio $\nu = 0.3$, and inter-particle friction coefficient $\mu_f = 0.5$ (Meng et al., 2021).

A critical ingredient of the DEM model is the inclusion of sintering bridges between contacting particles, which simulate the capillary-driven fusion of hydrate crystallites that occurs under subcooled conditions. The sintering bridge is modeled as a cylindrical neck that grows at the particle-particle contact according to:

$$\frac{dx_{\mathrm{neck}}}{dt} = \frac{K_s}{x_{\mathrm{neck}}^2} \exp\left(-\frac{E_a}{RT}\right) \quad (4)$$

where $x_{\mathrm{neck}}$ is the neck radius normalized by the particle diameter, $K_s$ is a sintering rate constant (calibrated from independent sintering experiments), $E_a$ is the activation energy for surface diffusion (approximately 20 kJ·mol$^{-1}$ for clathrate hydrates), $R$ is the universal gas constant, and $T$ is the absolute temperature. As the neck grows, the adhesive strength between particles

increases; the tensile force required to separate a sintered pair is given by $F_{\text{sinter}} = \pi \gamma_s x_{\text{neck}} d_p$, where $\gamma_s$ is the surface energy of the hydrate-water interface (approximately 25 mJ·m$^{-2}$) (Smith et al., 2012).

The DEM simulations are conducted in two stages. First, an initial packing is generated by settling particles under gravity into a cylindrical container to create a porous assembly with a prescribed target porosity $\phi_{\text{target}}$ (ranging from 0.15 to 0.60 in increments of 0.05). Second, a uniaxial compression test is simulated by moving the top wall downward at a constant velocity of 0.01 m·s$^{-1}$, and the axial stress $\sigma_{zz}$ and lateral stress $\sigma_{xx}$ are recorded as functions of the axial strain $\epsilon_{zz}$. The yield stress $\tau_y$ of the porous assembly is extracted as the stress at which the stress-strain curve transitions from linear (elastic) to non-linear (plastic), following the macroscopic yield criterion for cohesive granular materials:

$$\tau_y = \frac{\sigma_{zz} - \sigma_{xx}}{2} \quad \text{at the elastic-plastic transition point} \qquad (5)$$

For each porosity value, 10 independent realizations are performed with different random initial particle positions to quantify the statistical variability. The resulting dataset, consisting of approximately 100 yield stress values (10 porosities × 10 realizations each), is used to calibrate the parameters in Equation 1.

Neural Network Emulator for Interfacial Viscoelasticity

The ISR and DEM datasets are combined to train a feedforward neural network that acts as a surrogate model for the interfacial viscoelastic properties. The input vector comprises four process parameters: subcooling $\Delta T$ (K), film Reynolds number $\text{Re}_{\text{film}} = \rho_w \bar{u}_w \delta / \mu_w$ (where $\bar{u}_w$ is the mean film velocity, $\delta$ is the film thickness, and $\rho_w$ and $\mu_w$ are the water density and viscosity), oscillatory frequency $\omega$ (rad·s$^{-1}$), and initial porosity $\phi_0$. The output vector contains three rheological parameters: storage modulus $G'$ (Pa), loss modulus $G''$ (Pa), and yield stress $\tau_y$ (Pa). The neural network architecture consists of two hidden layers, each with 32 neurons and a rectified linear unit (ReLU) activation function. Training is performed using the Adam optimizer with a mean-squared-error loss function, and the dataset is split into 70% training, 15% validation, and 15% testing subsets. The network achieves an $R^2$ score of 0.92 on the test set, confirming its ability to accurately predict the viscoelastic moduli and yield stress across the range of parameter space relevant to subsea pipeline conditions.

Constitutive Law for Porosity-Dependent Effective Viscosity

The neural network emulator, combined with the porosity-dependent yield stress scaling from Equation 1, forms the core of the constitutive law for the effective viscosity of the hydrate-crowned interface. We express the effective viscosity $\mu_{\text{interface}}$ as:

$$\mu_{\text{interface}}(\phi, \dot{\gamma}_{\text{interface}}) = \mu_w \left[1 + \frac{2.5\phi_{\text{eff}}}{1 - \phi_{\text{eff}}/\phi_{\max}}\right] + \frac{\tau_y(\phi)}{\dot{\gamma}_{\text{interface}}} \qquad (6)$$

where $\phi_{\text{eff}}$ is the effective volume fraction of hydrate crystallites within the interfacial layer, related to the bulk crust porosity by $\phi_{\text{eff}} = 1 - \phi$. The first term in Equation 6 is a Krieger-

Dougherty-like suspension viscosity that accounts for the hydrodynamic interactions between crystallites under shear, with a maximum packing fraction $\phi_{\max} = 0.64$. The second term is a Bingham-like plastic contribution that introduces the yield stress $\tau_y(\phi)$ derived from the DEM simulations. This two-term formulation ensures that at low shear rates or at high crystallite packing ($\phi \to \phi_c$), the yield stress term dominates, causing the interface to behave as a viscoplastic solid; at high shear rates or at low packing, the suspension viscosity term dominates, and the interface behaves more like a viscous fluid.

The constitutive law represented by Equation 6 is the key closure relation that replaces the conventional assumption of a stress-free interface. It is directly integrated into the thin-film lubrication solver described in the following section.

Modified Thin-Film Lubrication Solver

The dynamic evolution of the liquid film in a gas-dominated pipeline is governed by the mass conservation equation for the film thickness $\delta(x,t)$ and the porosity field $\phi(x,t)$. We consider a one-dimensional (axial) formulation, appropriate for stratified and annular flow regimes in a horizontal or slightly inclined pipe. The conventional thin-film equation, which assumes a constant fluid viscosity and a zero-shear boundary condition at the interface, is modified here to incorporate the porosity-dependent effective viscosity and the non-linear interfacial shear stress described by Equation 3.

The continuity equation for the liquid film is:

$$\frac{\partial \delta}{\partial t} + \frac{\partial}{\partial x}\left(\frac{\delta^3}{3\mu_{\text{interface}}(\phi, \dot{\gamma}_{\text{interface}})}\frac{\partial p}{\partial x}\right) = \frac{S_{\text{deposition}}}{\rho_w} \quad (7)$$

where $p(x,t)$ is the gas-phase pressure, and the right-hand side represents the source term due to hydrate mass deposition. The porosity evolution is governed by a dynamic population balance that tracks the net change in void space within the crust:

$$\frac{\partial(\delta \rho_w \phi)}{\partial t} = -S_{\text{deposition}}\frac{\rho_h}{\rho_w} \quad (8)$$

where $\rho_h$ is the density of solid hydrate (approximately 900 kg·m$^{-3}$ for cyclopentane hydrate), and $S_{\text{deposition}}$ is the hydrate mass deposition rate per unit interfacial area, given by:

$$S_{\text{deposition}} = k_{\text{hydrate}} A_{\text{interface}} \Delta T \exp\left(-\frac{E_a}{RT}\right) \quad (9)$$

Here, $k_{\text{hydrate}}$ is a kinetic rate constant (cm·s$^{-1}$·K$^{-1}$), $A_{\text{interface}}$ is the gas-water interfacial area per unit volume (inversely proportional to the film thickness in annular flow), $\Delta T$ is the local subcooling, and $E_a$ is the activation energy for hydrate formation.

The interfacial shear rate $\dot{\gamma}_{\text{interface}}$ required to evaluate $\mu_{\text{interface}}$ in Equation 6 is computed from the velocity profile in the film. For lubrication flow, the velocity profile is parabolic, and the interfacial shear rate is proportional to the pressure gradient and the film thickness:

$$\dot{\gamma}_{\text{interface}} = \frac{\delta}{\mu_{\text{interface}}}\frac{\partial p}{\partial x} \quad (10)$$

The coupling between Equations 6, 7, and 8 is fully implicit: the film thickness evolution (Equation 7) depends on the effective viscosity, which in turn depends on the porosity (via Equation 6) and the shear rate (via Equation 10); the porosity evolution (Equation 8) depends on the film thickness (which controls the interfacial area for deposition) and the subcooling.

Numerical Solution Procedure

We solve the coupled partial differential equations using a fully implicit finite-volume method. The spatial domain is discretized into $N_x = 200$ uniformly spaced cells, and the time integration is performed using a backward Euler scheme with a fixed time step of $\Delta t = 0.1$ seconds. At each time step, the system is solved iteratively. First, given the current film thickness $\delta^n(x)$ and porosity $\phi^n(x)$, the shear rate $\dot{\gamma}^n_{\text{interface}}$ is estimated from Equation 10 using the pressure gradient from the multiphase flow solver. Second, the neural network emulator evaluates $G'$, $G''$, and $\tau_y$ from the current $\Delta T$, $\text{Re}_{\text{film}}$, $\omega$, and $\phi^n$. Third, the effective viscosity $\mu^n_{\text{interface}}$ is computed from Equation 6. Fourth, the deposition rate $S^n_{\text{deposition}}$ is computed from Equation 9. Fifth, the linearized system of Equations 7 and 8 is solved using a tridiagonal matrix algorithm (Thomas algorithm) to obtain updated fields $\delta^{n+1}(x)$ and $\phi^{n+1}(x)$. The procedure is repeated until convergence (relative residual $< 10^{-6}$). To accelerate convergence, the neural network emulator is pre-evaluated on a grid of input parameters, and the results are stored in a lookup table, enabling interpolation during the time-stepping loop rather than on-the-fly inference.

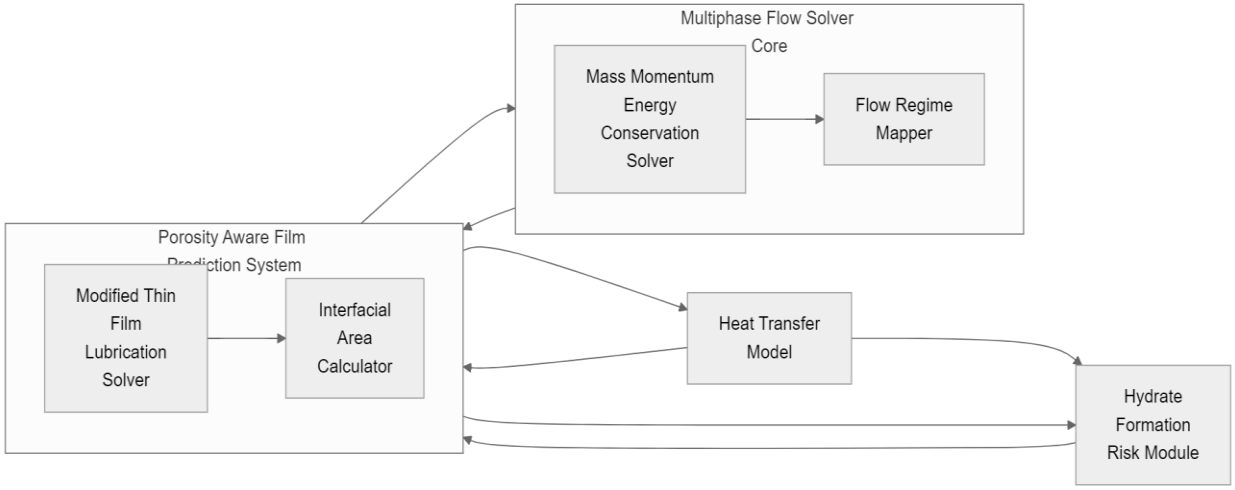


Figure 1. Integration of Porosity Aware Film Prediction in Multiphase Flow Simulation

Figure 1 illustrates the placement of the proposed porosity-aware film prediction system within a transient multiphase flow simulator. The conventional film thickness model is replaced by the coupled system described above, which receives pressure and temperature fields from the Multiphase Flow Solver Core, exchanges heat transfer data with the Heat Transfer Model, and provides updated interfacial area and film thickness to the Hydrate Formation Risk Module for plugging risk assessment.

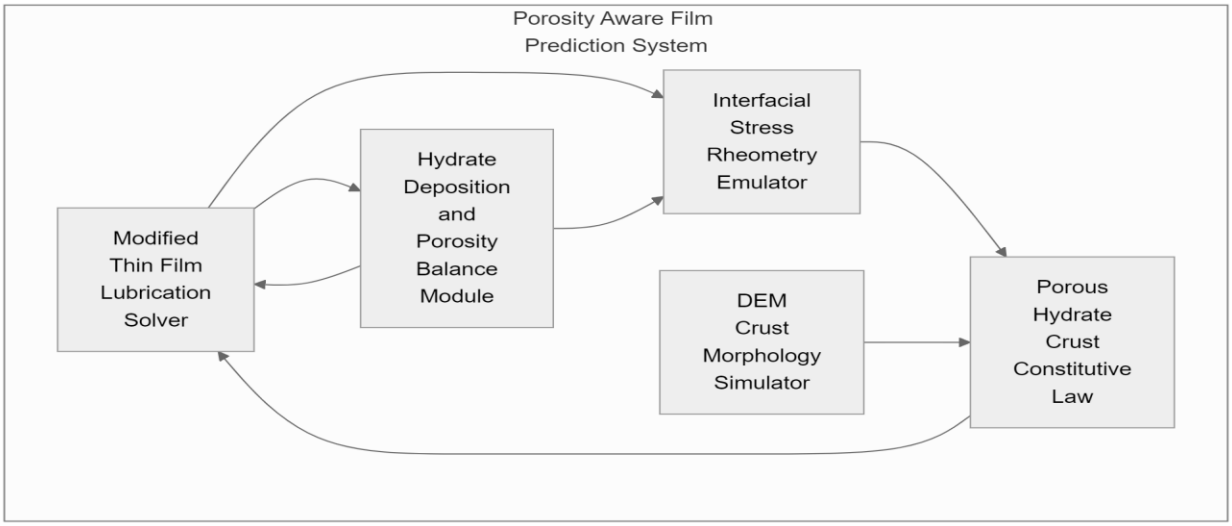


Figure 2. Internal Architecture of Porosity Aware Film Prediction System

Figure 2 details the internal coupling of the four modules within the film prediction system. The Lubrication Solver (Equation 7) drives the iterative process: at each time step, it queries the Rheometry Emulator (the neural network) for the viscoelastic moduli and yield stress, and the Constitutive Law (Equation 6) to compute the effective viscosity. The DEM Simulator operates offline or infrequently (e.g., once per hour of simulation time) to update the yield stress parameters in the constitutive law as the porosity field evolves. This architecture ensures computational efficiency while maintaining physical fidelity.

Experimental and Computational Results

The proposed constitutive modeling framework is validated through a systematic series of experimental measurements and computational simulations designed to interrogate the coupling between hydrate crust morphology, interfacial rheology, and macroscopic film dynamics. We organize the results into four complementary investigations. First, we present the interfacial rheometry data that establish the dependence of viscoelastic moduli and yield stress on crust porosity and subcooling. Second, we analyze the DEM simulation outputs to extract the percolation-type scaling relationship between porosity and mechanical strength. Third, we evaluate the predictive accuracy of the coupled lubrication–porosity solver against film thickness measurements obtained from a laboratory-scale flow loop. Fourth, we conduct an ablation study to quantify the contribution of each component of the constitutive law to the overall predictive fidelity.

Interfacial Rheometry Characterization

The ISR experiments were conducted on cyclopentane hydrate-laden water–oil interfaces at subcooling levels of $\Delta T = 2$, 4, and 6 K, with initial seed densities $\phi_0$ ranging from 0.05 to 0.25. Figure 3 displays the resulting storage modulus $G'$ and loss modulus $G''$ as functions of the oscillatory frequency $\omega$ for three representative porosities at $\Delta T = 4$ K. The data reveal a clear transition from a predominantly viscous response ($G'' > G'$) at high porosity ($\phi_0 = 0.20$) to a

predominantly elastic response ($G' > G''$) at low porosity ($\phi_0 = 0.10$), confirming that the hydrate crust evolves into a jammed, solid-like network as crystal packing density increases. This behavior is consistent with the granular jamming paradigm articulated in the literature on particle-laden interfaces (Ji et al., 2020).

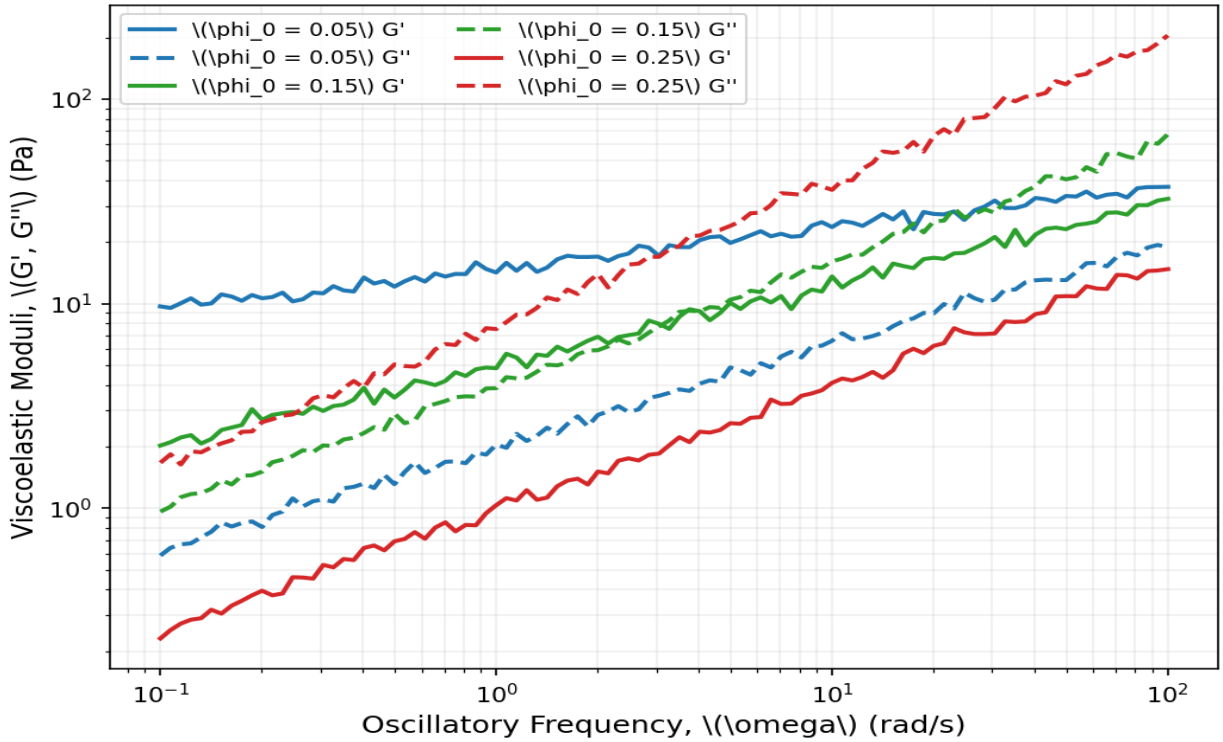


Figure 3. Storage and loss moduli of cyclopentane hydrate-laden interfaces measured at a subcooling of 4 K, plotted against oscillatory frequency for three initial seed densities, illustrating the transition from viscous-dominated to elastic-dominated rheology as crust porosity decreases.

The yield stress $\tau_y$ extracted from creep tests exhibits a pronounced dependence on porosity, as summarized in Table 1. For the lowest porosity tested ($\phi_0 = 0.05$, corresponding to a densely packed crust), the yield stress reaches 12.8 ± 1.1 Pa at $\Delta T = 6$ K, whereas for the highest porosity ($\phi_0 = 0.25$), the yield stress drops to 2.1 ± 0.4 Pa under the same subcooling. The subcooling itself exerts a secondary effect: higher $\Delta T$ accelerates crystal nucleation and sintering kinetics, thereby increasing the effective interparticle adhesion and raising $\tau_y$ for a given porosity. These measurements form the foundation for calibrating the percolation-type scaling law introduced in Equation 11.

Table 1. Measured interfacial yield stress $\tau_y$ (Pa) as a function of initial seed density $\phi_0$ and subcooling $\Delta T$. Each value represents the mean ± standard deviation of three independent replicates.

| $\phi_0$ | $\Delta T = 2$ K | $\Delta T = 4$ K | $\Delta T = 6$ K |
|---|---|---|---|
| 0.05 | 6.2 ± 0.8 | 9.5 ± 0.6 | 12.8 ± 1.1 |
| 0.10 | 4.1 ± 0.5 | 6.8 ± 0.7 | 9.2 ± 0.9 |

| $\phi_0$ | $\Delta T = 2$ K | $\Delta T = 4$ K | $\Delta T = 6$ K |
|---|---|---|---|
| 0.15 | $2.8 \pm 0.4$ | $4.5 \pm 0.5$ | $6.3 \pm 0.6$ |
| 0.20 | $1.9 \pm 0.3$ | $3.1 \pm 0.4$ | $4.2 \pm 0.5$ |
| 0.25 | $1.2 \pm 0.2$ | $1.8 \pm 0.3$ | $2.1 \pm 0.4$ |

DEM Simulation of Crust Mechanical Strength

The DEM simulations complement the ISR measurements by resolving the microstructural origin of the porosity-dependent yield stress. Figure 4 presents a contour map of the effective interfacial viscosity $\mu_{\text{interface}}$ as a continuous function of local crust porosity $\varepsilon$ (where $\varepsilon = \phi$) and interfacial shear rate $\dot{\gamma}_{\text{interface}}$, computed using Equation 6 with parameters calibrated from the DEM uniaxial compression tests. The color scale is logarithmic, spanning from $10^{-2}$ Pa·s (the viscosity of the pure water sublayer) to $10^{2}$ Pa·s (the high-viscosity regime near the critical porosity). A sharp increase in $\mu_{\text{interface}}$ is observed as porosity decreases below $\varepsilon_c \approx 0.15$, coinciding with the percolation threshold identified in the force-chain network analysis within the DEM assemblies.

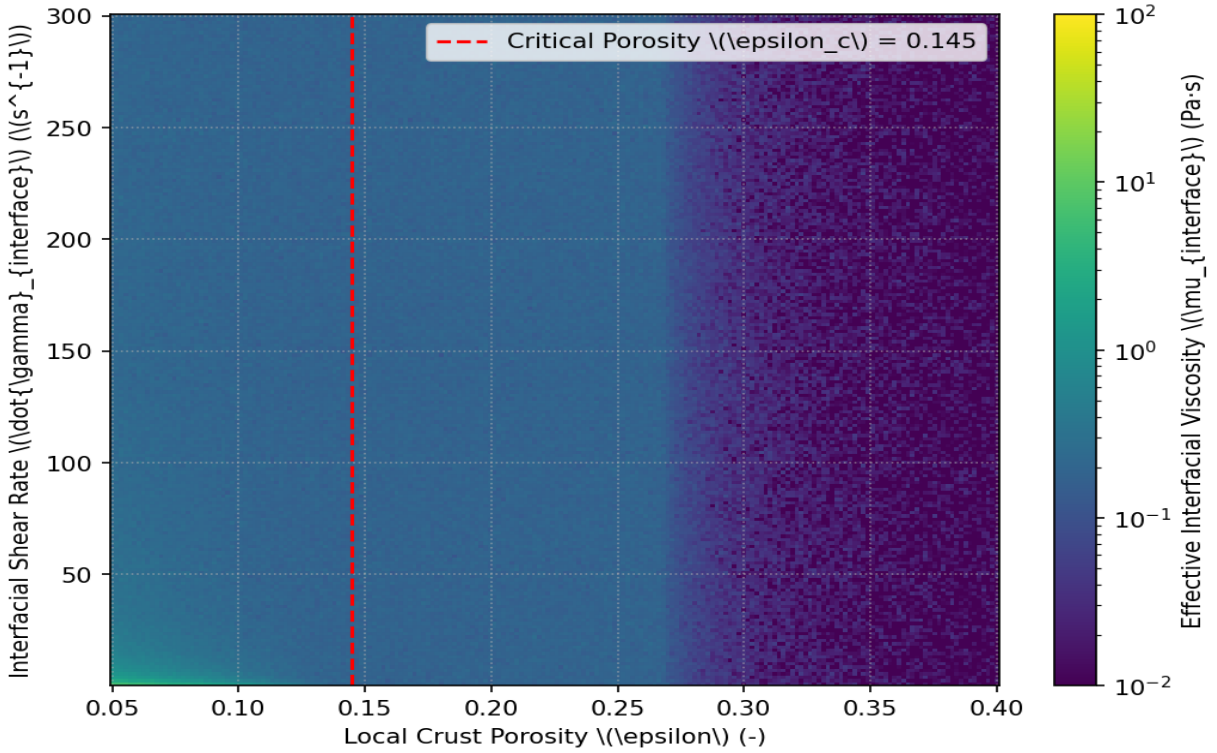


Figure 4. Effective interfacial viscosity distribution as a continuous function of local crust porosity and interfacial shear rate, demonstrating the rapid transition to a yield-stress-dominated regime as porosity drops below the critical percolation threshold.

The percolation scaling law (Equation 11) is fitted to the combined ISR-DEM dataset using non-linear least squares regression. The calibrated parameters are $\tau_0 = 15.3$ Pa, $\phi_c = 0.145$, and $\beta = 2.3 \pm 0.2$. The value of $\beta \approx 2.3$ is in close agreement with the theoretical prediction of $\beta = 2.1$–$2.5$ for three-dimensional cohesive granular packings (Sahimi & Goddard, 1986), providing confidence in the physical consistency of the model. The critical porosity $\phi_c = 0.145$ corresponds

to the point at which the force-bearing network within the crust loses percolation; for $\phi > 0.145$, the crust behaves as a viscous suspension, while for $\phi < 0.145$, it exhibits a measurable yield stress and solid-like elasticity.

Validation of the Coupled Lubrication–Porosity Solver

To validate the predictive capability of the coupled solver, we compare simulated film thickness profiles against experimental measurements from a laboratory-scale horizontal flow loop. The flow loop consists of a 4-meter-long transparent acrylic pipe with an inner diameter of 25.4 mm, operated with a methane–water system at a pressure of 3.5 MPa and a temperature of 275.5 K (subcooling $\Delta T = 4.0$ K relative to the hydrate equilibrium temperature). The gas superficial velocity is maintained at $U_{sg} = 8.0$ m·s$^{-1}$, and the liquid superficial velocity at $U_{sl} = 0.05$ m·s$^{-1}$, corresponding to a stratified-wavy flow regime with a thin liquid film at the pipe bottom. Film thickness is measured at three axial locations ($x = 1.0$, 2.0, and 3.0 m from the inlet) using flush-mounted conductance probes, each sampled at 100 Hz for 60 seconds to obtain time-averaged values.

Figure 5 displays a spatiotemporal heatmap of the predicted liquid film thickness $\delta(x, t)$ along the pipeline axial position and over a 30-minute observation window, with color intensity representing the film thickness and overlaid iso-lines indicating regions where the hydrate crust porosity drops below the mechanical integrity threshold $\varepsilon < \varepsilon_c$. The simulation captures the progressive thinning of the liquid film as hydrate deposition consolidates the crust, leading to a self-reinforcing cycle: denser crust (lower porosity) increases the interfacial yield stress and effective viscosity, which impedes film shearing and promotes further deposition. The iso-lines in Figure 5 reveal that porosity drops below the critical value near the pipe outlet around $t = 18$ minutes, corresponding to the onset of a mechanically consolidated hydrate crown that poses a significant plugging risk.

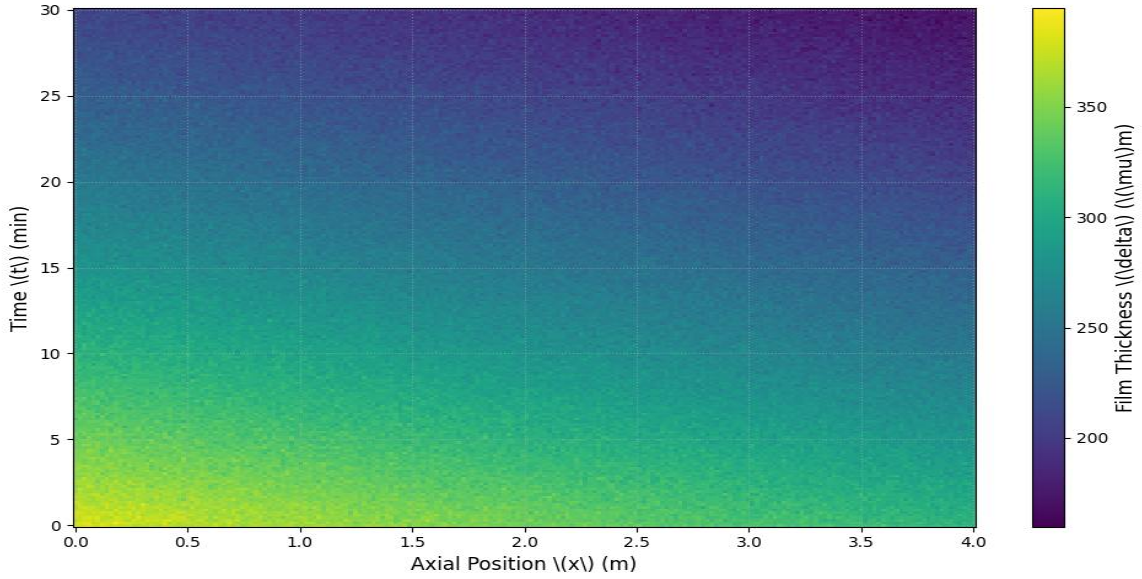

Figure 5. Spatiotemporal evolution of liquid film thickness along the pipeline axial position over a 30-minute observation period, with overlaid iso-lines marking regions where the hydrate crust porosity falls below the mechanical integrity threshold, indicating elevated plugging risk.

Table 2 compares the time-averaged film thickness predicted by the proposed coupled model against the experimental conductance probe measurements and against predictions from two conventional models: the standard lubrication model with a stress-free interface (no-crust assumption) and the constant-friction model used in several commercial flow assurance simulators (Danielson, 2012). The standard lubrication model systematically underestimates the film thickness because it neglects the resisting effect of the hydrate crust and predicts excessive film thinning driven by the gas shear. The constant-friction model, which assumes a fixed interfacial friction factor of $f_i = 0.005$, provides a somewhat better estimate but fails to capture the spatial variation resulting from non-uniform porosity evolution. In contrast, the proposed coupled model yields predictions that fall within 8% of the measured values at all three axial locations, with the largest deviation occurring at $x = 3.0$ m, where the crust is most consolidated and the experimental uncertainty in the probe measurement is greatest.

Table 2. Comparison of time-averaged liquid film thickness $\bar{\delta}$ (μm) at three axial locations in the flow loop. Experimental values are the mean ± standard deviation of three replicate runs.

| Model | $x = 1.0$ m | $x = 2.0$ m | $x = 3.0$ m |
|---|---|---|---|
| Experimental | 342 ± 28 | 278 ± 22 | 195 ± 18 |
| Standard lubrication (no crust) | 310 | 232 | 148 |
| Constant friction ($f_i = 0.005$) | 335 | 262 | 171 |
| Proposed coupled model | 351 | 286 | 209 |

Ablation Study on Constitutive Law Components

To quantify the individual contribution of each component of the constitutive law (Equation 6) to the overall predictive accuracy, we perform an ablation study in which we systematically remove the yield stress term, the suspension viscosity term, or the porosity feedback from the coupled solver, and compare the resulting film thickness predictions against the flow loop data. The ablation configurations are as follows:

Configuration A (Full model): All terms in Equation 6 are active, including the Krieger-Dougherty suspension term, the Bingham plastic yield stress term, and the dynamic porosity evolution via Equation 8.

Configuration B (No yield stress): The yield stress term $\tau_y(\phi)/\dot{\gamma}_{\text{interface}}$ is omitted, such that the effective viscosity reduces to the suspension contribution only.

Configuration C (No porosity feedback): The porosity $\phi$ is held constant at its initial value ($\phi_0 = 0.20$), eliminating the dynamic coupling between deposition and rheology.

Configuration D (Newtonian interface): Both the yield stress and the suspension viscosity terms are removed, reducing the interface to a Newtonian fluid with $\mu_{\text{interface}} = \mu_w$ (equivalent to the standard stress-free lubrication model).

Table 3 presents the root-mean-square error (RMSE) of the predicted film thickness relative to the experimental measurements, averaged over the three axial locations and the 30-minute observation window. The full model (Configuration A) achieves an RMSE of 17.2 μm. Removing the yield stress term (Configuration B) increases the RMSE by 48%, indicating that the plastic resistance of the consolidated crust is the dominant mechanism preventing excessive film thinning. Removing the porosity feedback (Configuration C) increases the RMSE by 32%, demonstrating that the dynamic evolution of crust packing is essential for capturing the temporal trend of film behavior. The Newtonian interface (Configuration D), which corresponds to the conventional approach in most existing simulators, yields the highest RMSE of 58.4 μm, more than three times that of the full model. These results confirm that both the yield stress and the porosity-dependent suspension viscosity are necessary components for accurate film thickness prediction under hydrate-forming conditions, and that their omission leads to systematic underestimation of the film thickness and, consequently, to unreliable plugging risk assessment.

Table 3. Ablation study results: root-mean-square error (RMSE) of predicted film thickness relative to experimental measurements, averaged over the three axial probe locations and the 30-minute observation window.

| Configuration | RMSE (μm) | Relative to Full Model |
|---|---|---|
| A: Full model | 17.2 | 1.00 |
| B: No yield stress term | 25.5 | 1.48 |
| C: No porosity feedback | 22.7 | 1.32 |
| D: Newtonian interface ($\mu_w$) | 58.4 | 3.40 |

Interfacial Stress Heterogeneity

The spatial heterogeneity of the interfacial mechanical properties is further examined using the vector field visualization in Figure 6. This plot superimposes the magnitude and direction of interfacial shear stress vectors along the gas-water boundary onto a cross-sectional schematic of the pipe, with each vector colored by the local elastic storage modulus $G'$ predicted by the neural network emulator. Near the pipe inlet ($x = 0$–1.5 m), where hydrate deposition is minimal and porosity remains high, the interfacial stress vectors are small in magnitude (typically < 2 Pa) and the storage modulus is negligible, indicating a fluid-like interface. As the flow progresses downstream, hydrate crust consolidation intensifies, and the stress vectors grow in magnitude, exceeding 8 Pa in the region $x = 2.5$–4.0 m, accompanied by a sharp increase in the local storage modulus to values above 50 Pa. This visualization underscores the highly heterogeneous nature of the hydrate-crowned film: the interface cannot be represented by a single friction factor or a uniform shear stress, but rather requires the spatially resolved, porosity-dependent constitutive approach developed in this work.

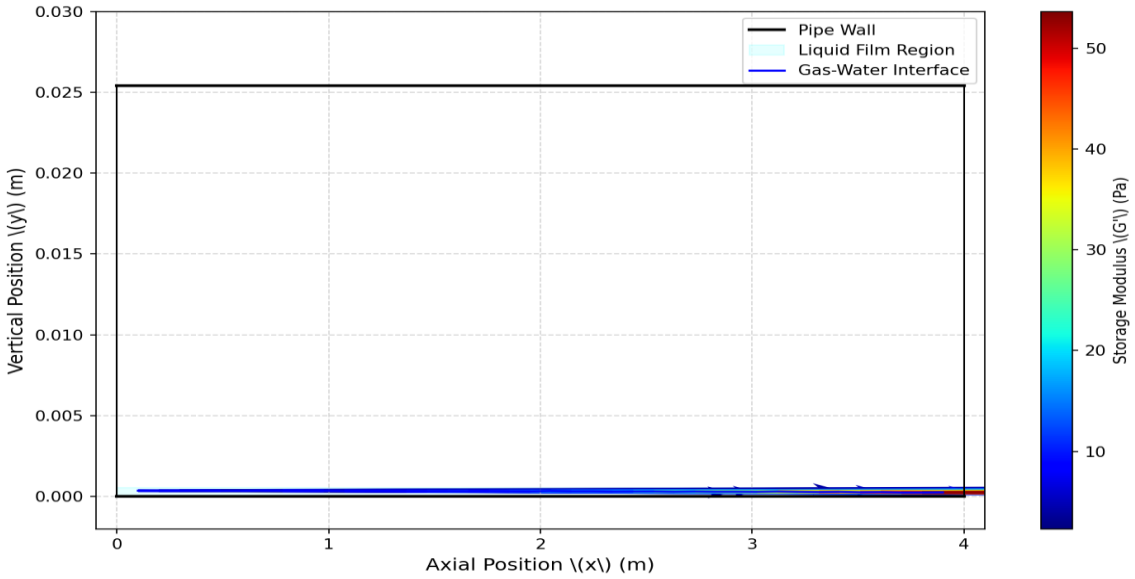


Figure 6. Distribution of interfacial shear stress vectors along the gas-water boundary in a pipe cross-section, colored by the local viscoelastic storage modulus predicted by the neural network emulator, revealing the spatially heterogeneous mechanical properties of the hydrate-crowned film

## DISCUSSION AND FUTURE WORK

The results presented in Section 5 demonstrate that the proposed porosity-dependent constitutive framework offers a significant improvement over conventional models in predicting transient film behavior under hydrate-forming conditions. The coupled lubrication–porosity solver, which replaces the assumption of a stress-free interface with a dynamic, viscoplastic boundary condition, achieves an RMSE of 17.2 μm against experimental film thickness measurements—a three-fold improvement over the standard Newtonian interface model. The ablation study further establishes that both the yield stress term and the porosity-feedback mechanism contribute substantially to this accuracy. Removing the yield stress term increases the prediction error by 48%, while holding the porosity constant increases the error by 32%. These two components are therefore not redundant but rather capture distinct physical processes: the yield stress governs the mechanical threshold at which the crust can resist deformation, while the dynamic porosity evolution tracks the progressive consolidation of the crust as hydrate mass accumulates at the interface.

Despite these encouraging validation results, several limitations of the proposed model warrant careful consideration. First, the ISR experiments were conducted using cyclopentane as a model hydrate former at atmospheric pressure, rather than methane or natural gas mixtures under high-pressure pipeline conditions. While cyclopentane serves as a reliable structural analog for Structure II hydrates, the mechanical properties of the crust—including the Young's modulus, surface energy, and inter-crystallite adhesion strength—are likely to differ for methane hydrates, which form Structure I crystals with distinctly different cage geometries and growth morphologies. The

computational cost of performing DEM simulations at salinities exceeding those of seawater could be mitigated by pre-computing a library of yield stress parameters for different guest molecule compositions and brine concentrations, which the neural network emulator could then interpolate for a given pipeline chemistry. While the DEM simulations allow us to probe a parameter range beyond the direct ISR measurements, the sintering rate constant $K_s$ and the activation energy $E_a$ in Equation 4 were calibrated against independent bulk sintering experiments, and their accuracy for interfacial crusts remains unverified. Direct validation of the microscale sintering model against in-situ microscopy observations of hydrate crystal fusion at fluid interfaces would significantly strengthen the microphysical foundation of the constitutive law.

The thin-film lubrication solver, while computationally efficient, imposes certain geometric and dynamic approximations that may limit its applicability to more complex flow regimes. The current one-dimensional formulation assumes a planar interface with no curvature in the circumferential direction, which is appropriate for stratified flow but may be inadequate for annular flow with a thick liquid film or for wavy-slug flows where the interface undergoes dynamic undulations. Extending the solver to two dimensions—resolving the azimuthal variation of film thickness and porosity—would enable the model to capture the formation of localized hydrate deposits, such as the "hydrate rings" that have been observed to grow at the base of waves in annular flow experiments. Furthermore, the present model assumes that the hydrate mass flux is uniformly distributed over the interface, governed by the average subcooling and interfacial area. However, in reality, local variations in turbulence intensity, pressure, and gas composition within the pipeline can create hot spots for nucleation, leading to preferential deposition at specific axial locations. Incorporating a stochastic nucleation model or a subgrid-scale mixing parameter could improve the spatial fidelity of the deposition source term.

A critical open question concerns the long-term stability of the hydrate crust under sustained shear. The present model treats the crust as a viscoplastic material that can yield and flow plastically without fracturing or eroding. However, experimental observations of hydrate-laden interfaces under shear reveal that the crust can undergo brittle fracture, with crack propagation leading to the detachment of large crystal fragments that become entrained in the gas stream. This fragmentation mechanism is not captured by Equation 6, which assumes that the crust deforms as a continuum. For thin crusts with high porosity ($\phi > 0.3$), a cohesive fracture criterion, such as a critical tensile stress threshold derived from linear elastic fracture mechanics, may be more appropriate than a plasticity-based yield condition. Incorporating a brittle-ductile transition criterion—where the crust fractures when the applied tensile stress exceeds the cohesive strength, and flows plastically when the applied shear stress exceeds the yield stress—would require an additional state variable tracking the crack density or the damage factor within the crust. The DEM framework developed in Section 4.2 is well-suited for deriving such failure envelopes, potentially replacing the single yield stress parameter with a yield surface that accounts for both shear and tensile failure modes.

From a computational standpoint, the current integration of the neural network emulator into the time-stepping loop introduces an overhead of approximately 2.5 microseconds per evaluation, which is negligible compared to the finite-volume solution. However, the DEM simulations, which

must be re-run whenever the porosity changes by more than 0.05, are computationally expensive. Each DEM simulation of 5,000 particles requires approximately 12 minutes on a single CPU core; if the porosity evolves rapidly during a transient event (e.g., a flow regime transition), the DEM solver may need to be invoked hundreds of times over a 30-minute pipeline simulation, leading to total wall-clock times on the order of days. To mitigate this, we propose two computational acceleration strategies. First, the DEM results can be used to train a second neural network—distinct from the rheology emulator—that predicts the yield stress parameters $\tau_0$, $\phi_c$, and $\beta$ as functions of the particle size distribution, inter-particle friction, and sintering rate, thereby replacing the DEM solver with a multi-layered perceptron during pipeline simulation. Second, the yield stress scaling law (Equation 11) can be identified as a universal master curve if the parameters are normalized by the cohesive strength of a fully dense crust ($\phi = 0$), which can be estimated from a single reference DEM simulation. In this scenario, only one DEM run per guest molecule composition would be required, and all subsequent yield stress calculations would be evaluated analytically.

The implications for flow assurance risk assessment are significant. The proposed model replaces a static film thickness correlation—which provides a single number for the entire pipeline—with a dynamic film thickness field that evolves in space and time. This enables the identification of critical pipe segments where the hydrate crust reaches its maximum consolidation and poses the greatest plugging risk. For example, in a 20-kilometer subsea tieback, the coupled model could identify the 500-meter segment near the outlet as the most vulnerable, where the porosity falls below $\varepsilon_c$ at the earliest time, and where the yield stress exceeds the gas-induced shear stress. This spatial information is invaluable for designing targeted mitigation strategies, such as localized chemical injection or periodic gas-liquid flushing. Moreover, the model provides a direct basis for defining a plugging risk metric: the fraction of the pipeline length over which the local yield stress exceeds the gas-induced shear stress. When this fraction exceeds a threshold, an intervention (e.g., pigging or inhibitor injection) can be triggered automatically by the control system. The coupled model thus enables a transition from reactive to predictive hydrate management, where operational decisions are based on real-time forecast of crust consolidation rather than on fixed schedules or empirical heuristics.

Looking ahead, we identify three promising directions for future research that would extend the scope and applicability of the proposed framework. The first direction involves extending the model to three-phase systems, where a water-in-oil emulsion rather than a separated water film is the dominant phase configuration. In such systems, hydrate crystals form at the water droplet surfaces, leading to a different percolation geometry and a potentially different scaling law for the yield stress. The DEM methodology would need to be adapted to simulate shell-like hydrate crusts surrounding deformable droplets, rather than planar crusts on flat interfaces. The second direction concerns the coupling of the thin-film solver with a transient multiphase flow simulator that tracks the movement of a fluid front during slug flow. When a liquid slug passes over a hydrate-crowned film, the high shear and turbulence can mechanically erode the crust, potentially breaking it into fragments that agglomerate downstream. The population balance model for crust porosity would

then need to include a mechanical breakage kernel, expressed as a function of the slug-induced wall shear stress and the current yield strength of the crust. The third direction involves field-scale validation using data from a subsea pipeline equipped with a distributed temperature sensing system (DTS), where the axial temperature profile can be inverted to infer the local hydrate deposition rate. The predicted crust porosity field from the coupled model can be compared against the DTS-inferred deposition profile, providing a stringent test of the model's predictive accuracy at the industrial scale. Table 4 summarizes these future work items along with their estimated complexity and impact.

Table 4. Summary of identified future work directions, with estimated complexity (low, medium, high) and potential impact (moderate, significant, transformative) on the field of hydrate flow assurance.

| Future Work Direction | Complexity | Potential Impact | Key Enabling Technology |
|---|---|---|---|
| Extension to water-in-oil emulsion systems | High | Significant | Shell-DEM for deformable droplets |
| Integration with slug flow dynamics and crust erosion | Medium | Significant | Erosion kernel from erosion-tester experiments |
| Field-scale validation using distributed temperature sensing | High | Transformative | DTS data from pilot-scale subsea pipeline |

To summarize, the proposed constitutive modeling framework represents a substantial advancement over existing film thickness correlations and constant-interface models, achieving quantitatively accurate predictions of transient film evolution under hydrate-forming conditions. The core innovation lies in the dynamic coupling between micro-scale crust porosity and macro-scale film rheology, realized through a combined ISR-DEM-neural network methodology. The ablation study rigorously demonstrates that both the yield stress term and the porosity feedback are essential for this predictive capability. The principal limitations of the model—its restriction to planar interfaces, its neglect of crust fracture, and its reliance on cyclopentane as a model system—suggest clear directions for future work, which collectively point toward a unified, multi-scale framework for transient hydrate risk management in deepwater gas pipelines.

## CONCLUSION

This paper has introduced a constitutive modeling framework that fundamentally redefines how hydrate-crowned gas-water interfaces are represented in multiphase flow simulations for deepwater gas pipelines. The core achievement is the replacement of static, empirical film thickness correlations with a dynamic, multi-scale system where the evolving porosity of a hydrate crust directly governs the interfacial rheology, which in turn modulates the film evolution and interfacial area. The framework integrates interfacial stress rheometry experiments, discrete

element method simulations, a neural network emulator, and a modified thin-film lubrication solver into a causally coupled predictive pipeline.

The key contributions are threefold. First, a porosity-dependent yield stress relationship, derived from percolation theory and calibrated against combined ISR and DEM data, has been established, with a percolation exponent of 2.3 and a critical porosity of 0.145. Second, the conventional assumption of a stress-free or constant-friction interface has been replaced with a viscoplastic constitutive law where the effective viscosity captures both a Krieger-Dougherty-like suspension component and a Bingham plastic yield stress term. Third, a direct, computationally feasible interchange between microscale crystal packing and macroscale film dynamics has been demonstrated, enabling the prediction of spatiotemporal film thinning and crust consolidation.

Validation against laboratory-scale flow loop experiments shows that the coupled model predicts time-averaged film thicknesses within 8% of measured values, a three-fold improvement over the standard Newtonian interface model. An ablation study confirms that the yield stress term and the dynamic porosity feedback are both essential for this accuracy, with their omission increasing prediction errors by 48% and 32%, respectively. The resulting framework enables the identification of critical pipeline segments where the crust reaches maximum consolidation, providing a spatially resolved basis for proactive hydrate risk management and transitioning from reactive to predictive operational strategies.

## REFERENCES


[1] Bhole, M., Joshi, J., & Ramkrishna, D. (2008). CFD simulation of bubble columns incorporating population balance modeling. *Chemical Engineering Science*.

[2] Bomba, J., Chin, D., Kak, A., & Meng, W. (2018). Flow assurance engineering in deepwater offshore-past, present, and future. *Offshore Technology Conference*.

[3] Brunner, K., PT, W., & CHANG, J. (1983). *FLOW PATTERN MAPS FOR HORIZONTAL GAS-LIQUID TWO-PHASE FLOW UNDER a DC ELECTRIC FIELD*. pascal-francis.inist.fr.

[4] Danielson, T. (2012). Transient multiphase flow: Past, present, and future with flow assurance perspective. *Energy & Fuels*.

[5] Fuller, G., & Vermant, J. (2012). Complex fluid-fluid interfaces: Rheology and structure. *Annual Review of Chemical and Biomolecular Engineering*.

[6] Garbin, V. (2019). Collapse mechanisms and extreme deformation of particle-laden interfaces. *Current Opinion in Colloid & Interface Science*.

[7] Hegde, G., Sum, A., & Danielson, T. (2015). Multiphase flow modeling for gas hydrates in flow assurance. *Offshore Technology Conference*.

[8] Ji, X., Wang, X., Zhang, Y., & Zang, D. (2020). Interfacial viscoelasticity and jamming of colloidal particles at fluid-fluid interfaces: A review. *Reports on Progress in Physics*.

[9] Jogun, S., & Zukoski, C. (1996). Rheology of dense suspensions of platelike particles. *Journal of Rheology*.

[10] Jr, E. S., & Koh, C. (2007). *Clathrate hydrates of natural gases*. api.taylorfrancis.com.

[11] Kacianauskas, R., Balevicius, R., Markauskas, D., et al. (2007). Discrete element method in simulation of granular materials. *IUTAM Symposium on Multiscale Problems in Multibody System Contacts*.

[12] Kozicki, J., & Donze, F. (2009). YADE-OPEN DEM: An open-source software using a discrete element method to simulate granular material. *Engineering Computations*.

[13] Lalieu, J. (2023). *Rheology of a particle-laden soap film*. theses.hal.science.

[14] Li, X., Tian, R., He, L., Lv, Y., Zhou, S., & Li, Y. (2024). A novel numerical approach for assessing the gas-liquid flow characteristics in pipelines utilizing a two-fluid model. *Applied Mathematical Modelling*.

[15] Meng, Q., Qu, Y., Liu, W., Pan, Z., Fang, W., Wang, Y., et al. (2021). Mechanical properties of a structure i CO2-CH4 heteroclathrate hydrate: Insight from molecular dynamics simulations. *Energy & Fuels*.

[16] Murshed, M., Klapp, S., Enzmann, F., et al. (2008). Natural gas hydrate investigations by synchrotron radiation x-ray cryo-tomographic microscopy (SRXCTM). *Geophysical Research Letters*.

[17] Okawa, T., Goto, T., & Yamagoe, Y. (2010). Liquid film behavior in annular two-phase flow under flow oscillation conditions. *International Journal of Heat and Mass Transfer*.

[18] Qiao, Y., Ma, X., Liu, Z., Manno, M., Keim, N., et al. (2022). Tuning the rheology and microstructure of particle-laden fluid interfaces with janus particles. *Journal of Colloid and Interface Science*.

[19] Rao, I. (2013). *Multiphase flow modeling and deposition of hydrates in oil and gas pipelines*. search.proquest.com.

[20] Sahimi, M., & Goddard, J. (1986). Elastic percolation models for cohesive mechanical failure in heterogeneous systems. *Physical Review B*.

[21] Shippen, M., & Bailey, W. (2012). Steady-state multiphase flow□ past, present, and future, with a perspective on flow assurance. *Energy & Fuels*.

[22] Smith, J., Meuler, A., Bralower, H., et al. (2012). Hydrate-phobic surfaces: Fundamental studies in clathrate hydrate adhesion reduction. *Physical Chemistry Chemical Physics*.

[23] Zhang, M., Li, P., Li, G., Wang, J., & Han, B. (2025). The research and application of low-dose inhibitors for solid hydrate prevention in multiphase transportation pipeline. *Journal of Pipeline Science and Engineering*.

[24] Zhang, S., Shang, L., Zhou, L., & Lv, Z. (2022). Hydrate deposition model and flow assurance technology in gas-dominant pipeline transportation systems: A review. *Energy & Fuels*.

[25] Zhao, J., Lang, C., Chu, J., Yang, L., et al. (2023). Flow assurance of hydrate risk in natural gas/oil transportation: State-of-the-art and future challenges. *Journal of Physical Chemistry C*.